

Identification of Source Terms in the Ginzburg-Landau Equation from Final Data

Roberto Morales* Javier Ramírez-Ganga†

Abstract

In this article, we study an inverse problem consisting in the identification of a space-time dependent source term in the Ginzburg-Landau equation from final-time observations. We adopt a weak-solution framework and analyze the associated Tikhonov functional, deriving an explicit gradient formula via an adjoint system and proving its Lipschitz continuity. We then establish existence and uniqueness results for quasi-solutions, and validate the theory with numerical experiments based on iterative methods.

Keywords: Inverse problem, Ginzburg-Landau equation, Numerical simulations.

MSC Classifications (2020): 35Q56, 35R30, 49N45, 65N21.

1 Introduction

This section introduces the mathematical formulation of the inverse problem and specifies the functional framework adopted throughout the paper. We also describe the model equation, its physical motivation, and the regularity assumptions required to ensure well-posedness.

Let $\Omega \subset \mathbb{R}^N$ be a bounded domain ($N \geq 1$) with boundary $\partial\Omega$ of class C^2 and $T > 0$. Here and in the sequel, the function spaces refer to spaces of complex-valued functions unless otherwise specified.

We consider a, b, \vec{r} and p with the following assumptions:

(H1) $a, b \in W^{1,\infty}(\Omega; \mathbb{R})$ with

$$a(x) \geq a_* > 0 \quad \text{almost everywhere in } \Omega,$$

for some a_* .

(H2) $\vec{r} = \vec{r}(x)$, $p = p(x)$ and $y_0 = y_0(x)$ are complex-valued functions such that

$$\vec{r} \in [W^{1,\infty}(\Omega)]^N, q \in L^\infty(\Omega) \text{ and } y_0 \in L^2(\Omega).$$

*Chair of Computational Mathematics, DeustoTech, University of Deusto, Avenida de las Universidades 24, Bilbao, 48007, Basque Country, Spain, e-mail: roberto.morales@deusto.es.

†Centro de Modelamiento Matemático (CMM) IRL 2807 CNRS-UChile and Departamento de Ingeniería Matemática (DIM), Universidad de Chile, Beauchef 851, Casilla 170-3, Correo 3, Santiago, Chile, e-mail: jramirez@dim.uchile.cl.

Now, consider the following Ginzburg-Landau equation with Dirichlet boundary conditions:

$$\begin{cases} \partial_t y - \operatorname{div}((a(x) + ib(x))\nabla y) + \vec{r}(x) \cdot \nabla y + p(x)y = f(x, t) & \text{in } \Omega \times (0, T), \\ y = 0 & \text{on } \partial\Omega \times (0, T), \\ y(\cdot, 0) = y_0 & \text{in } \Omega. \end{cases} \quad (1.1)$$

Under the assumptions **(H1)**, **(H2)** and $f \in L^2(0, T; L^2(\Omega))$, there exists a unique weak solution of (1.1) with the following regularity:

$$y \in C^0([0, T]; L^2(\Omega)) \cap L^2(0, T; H_0^1(\Omega)).$$

For completeness and self-containment, we include in Appendix A general statements, together with their proofs, concerning the existence of weak and strong solutions of the equation (1.1).

In this article, we will consider the following **Inverse Source Problem (ISP)**: Identify the unknown spatial-temporal source term f in the space $L^2(0, T; L^2(\Omega))$ in (1.1) from the following final time measured output:

$$u_T(x) := y(x, T), \quad x \in \Omega.$$

Here, $y(x, T) \equiv y(x, t)|_{t=T}$ is a trace appropriately defined of the weak solution $y(x, t)$ of (1.1). In addition, $u_T(x)$ represents the measured output containing a random noise.

Inverse source problems of this type are not only mathematically rich but also arise naturally in applied sciences. In many experimental settings, direct access to distributed sources is often impossible, and only partial or final-time measurements are available. For instance, in nonlinear optics one may measure the profile of a pulse at the end of a cavity, while the internal gain or loss mechanisms driving its formation remain hidden. Similarly, in chemical or biological pattern formation, one often observes the state of the system after some transient dynamics but seeks to infer the localized heterogeneities or forcing terms that generated it. This gap between accessible measurements and hidden dynamics motivates the study of reconstruction methods capable of identifying unknown excitations from indirect data.

The choice of the Ginzburg-Landau equation as the underlying model is particularly significant. It serves as a universal amplitude equation near the onset of instability in diverse physical systems, ranging from fluid dynamics and plasma physics to optics and chemical oscillations [2, 18, 6, 3, 19]. Consequently, advances in the understanding of inverse problems for this equation are not limited to a single discipline but carry implications across multiple fields. Identifying unknown sources in such a model not only enriches the theory of dissipative-dispersive PDEs but also provides a mathematical framework for interpreting experiments in which only end-point information is available.

At the mathematical level, the inverse source problem we consider is severely ill-posed. Regularization strategies and variational formulations thus become essential. Our work adopts this perspective, combining the theory of weak solutions, adjoint-based gradient formulas, and Tikhonov regularization to rigorously justify reconstruction algorithms and test their performance through numerical simulations.

1.1 Literature

We now review some representative contributions on the complex Ginzburg-Landau equation and its variants, emphasizing their role as canonical amplitude equations and discussing prior work related to inverse or identification problems.

The complex Ginzburg-Landau (GL) equation is the canonical amplitude equation near a Hopf or Turing-Hopf bifurcation. In its cubic form, it reads

$$\partial_t A = (\mu + i\omega)A + (1 + c_1 i)\Delta A - (1 + c_3 i)|A|^2 A,$$

while the cubic-quintic extension adds a saturating nonlinearity:

$$\partial_t A = (\mu + i\omega)A + (1 + c_1 i)\Delta A - (1 + c_3 i)|A|^2 A - (\nu + c_5 i)|A|^4 A,$$

with real parameters μ, ν, c_j ($j = 1, 3, 5$) that encode growth, dispersion/diffusion, and nonlinear gain/loss. The cubic model is the universal normal form near onset and captures phase diffusion, plane-wave selection and Benjamin-Feir/Newell instabilities. On the other hand, the quintic term become relevant farther from threshold to model saturation and complex dissipative structures (e.g. localized pulses). See the reviews [8] and [2], which also discuss higher-order variants and parameter scalings.

The cubic and cubic-quintic complex GL equations serve as canonical models of pattern formation and nonlinear wave dynamics in nonequilibrium systems. These models describe the slow complex envelope $A(x, t)$ of oscillatory modes near stability. In hydrodynamics and Rayleigh-Bénard convection, the cubic GL equation explains the emergence of roll patterns, travelling waves, and their stability domains [20] and [8]. In nonlinear optics, it governs mode-locked lasers, pulse propagation in fiber cavities, and the formation of dissipative solutions. In this case, the cubic-quintic equation extension accounts for gain saturation and quintic nonlinear effects that are essential for bounded amplitude states [23], [1]. Similarly, in chemical oscillations and biological excitable media, it models spiral waves, defect turbulence, and spatiotemporal chaos, highlighting its universality across disciplines [2].

From a mathematical viewpoint, the GL equations combine parabolic smoothing (via the Laplacian operator) with dispersive phase dynamics (via imaginary coefficients), which generates a delicate interplay between diffusion, dispersion, and nonlinearity [1, 8, 18, 19]. This hybrid character produces a wide spectrum of phenomena: existence of plane-wave solutions, modulational (Benjamin-Feir/Newell) instabilities, turbulence, and complex coherent structures [1, 8, 20, 23]. The cubic equation alone already yields chaotic attractors, defect-mediated turbulence, and spiral wave breakup [2, 3, 23], while the quintic term stabilizes or destabilizes localized patterns depending on parameter regimes [1, 23]. The GL equations have been used to study attractors, bifurcations, and long-time dynamics of nonlinear PDEs, serving as a testbed for methods in dissipative systems, control, and inverse problems [6, 19, 22, 4, 16].

Recovering sources and parameters in GL-type models is crucial in practice: in optics, it enables diagnosing distributed gain/loss or saturable absorbers in cavity models from end-of-pulse measurements; in chemical/biological pattern formation, it helps infer spatially localized forcing or heterogeneities driving wave patterns; in fluid and plasma contexts, it allows one to back-out effective forcing or feedback from limited snapshots near transitions to turbulence. Because the GL framework is a universal amplitude model, successful inversion translates across disciplines, providing interpretable maps of where and how energy is injected or dissipated. From a computational perspective, adjoint-based Tikhonov schemes scale to high-dimensional discretizations and accommodate realistic noise models [8], [2], [14].

Within this broad literature, inverse problems for GL-type models remain relatively less explored. Classical studies on inverse source problems for parabolic or Schrödinger-type equations [12, 13, 11, 7] provide methodological foundations, yet the adaptation to GL equations, which combine diffusion, dispersion, and nonlinearity, poses unique analytical and numerical challenges.

We also note that other GL-type models, such as those with dynamic boundary conditions, have recently attracted attention in the context of controllability [5]. While these studies highlight the

richness of the GL framework under more complex boundary interactions, the analysis of inverse problems in such settings remains largely open. Our contribution is thus complementary, as we address the identification of space-time dependent source terms for the standard GL equation, providing a first step toward broader inverse problem formulations in extended GL models.

It is worth emphasizing that the linear GL equation can also be expressed as a system of two coupled real-valued PDE equations, corresponding to the real and imaginary parts of the complex amplitude. In this formulation, the coupling terms are of second order and involve cross-derivative operators, which profoundly alter the analytical structure of the system. As a consequence, classical techniques from the theory of control and inverse problems for scalar parabolic equations (based on Carleman estimates and observability inequalities [10]) cannot be directly applied. In particular, the presence of complex coefficients and dispersive-type interactions requires adapted Carleman weights, refined energy estimates, and the development of new stability results tailored to mixed dissipative-dispersive operators.

The present work is intended as a first step toward a comprehensive theory of inverse problems for GL-type equations, focusing here on the standard setting with Dirichlet boundary conditions.

1.2 The input-output operator

To formalize the inverse problem, we introduce the input-output operator mapping the source term to the final-state of the system. This operator provides a compact representation of the forward model and allows for a variational reformulation of the inverse problem.

Let $\mathcal{U} \subset L^2(0, T; L^2(\Omega))$ be a non-empty set, which is supposed to be bounded, closed and convex. In addition, we define the operator $\Psi : \mathcal{U} \rightarrow L^2(\Omega)$ in the following way:

$$\Psi(f) = y(\cdot, T) \quad f \in \mathcal{U},$$

where $y = y(x, t)$ is the solution of (1.1) associated to the source term f .

We point out that, the **(ISP)** can be formulated in terms of Ψ as the following functional equation:

$$\Psi(f) = u_T(x), \quad x \in \Omega, \quad f \in \mathcal{U}. \quad (1.2)$$

We emphasize that, due to measurement errors in the output u_T , exact equality in the equation (1.2) cannot be satisfied in general. Moreover, we have the following result

Proposition 1.1. *The input-output operator $\Psi : L^2(0, T; L^2(\Omega)) \rightarrow L^2(\Omega)$ is compact.*

Proof. Let $(f_k)_{k \in \mathbb{N}}$ be a bounded sequence in $L^2(\Omega \times (0, T))$. Then, by Proposition A.3, the sequence of associated weak solutions $(y(\cdot, \cdot, f_k))_{k \in \mathbb{N}}$ is bounded in $C^0([0, T]; H_0^1(\Omega))$. In particular, the sequence $(Y_k)_{k \in \mathbb{N}}$ given by $Y_k := y(\cdot, T, f_k)$ is bounded in $H_0^1(\Omega) \cap H^2(\Omega)$. Thus, using the Sobolev-Gagliardo-Nirenberg compact embedding $H_0^1(\Omega) \hookrightarrow L^2(\Omega)$, there exists a subsequence of $(Y_k)_{k \in \mathbb{N}}$ which converges strongly in $L^2(\Omega)$. This implies that the input-output operator Ψ is compact and the proof of Proposition 1.1 is finished. \square

In view of the Proposition 1.1, it is evident that the inverse problem **(ISP)** is ill-posed in the sense of Hadamard. For this reason, one needs to introduce the functional $\mathcal{J} : \mathcal{U} \rightarrow \mathbb{R}$ by

$$\mathcal{J}(f) := \frac{1}{2} \int_{\Omega} |\Psi(f) - u_T|^2 dx, \quad (1.3)$$

and reformulate **(ISP)** in terms of the quasi-solution method, i.e., we minimize the following extremal problem

$$\mathcal{J}(f^*) = \inf_{f \in \mathcal{U}} \mathcal{J}(f).$$

Since the operator Ψ is compact, small perturbations in the data may cause large variations in the reconstructed source. Therefore, regularization becomes essential to obtain stable approximations. In this context, it is customary to consider a regularized Tikhonov version of the functional J in (1.3). For $\epsilon > 0$, we introduce the regularized functional

$$\mathcal{J}_\epsilon(f) := \frac{1}{2} \int_{\Omega} |\Psi(f) - u_T|^2 dx + \frac{\epsilon}{2} \int_0^T \int_{\Omega} |f|^2 dx dt, \quad f \in \mathcal{U}. \quad (1.4)$$

1.3 Outline

The rest of the paper is as follows. In Section 2, we focus on the properties of J , i.e., a detailed characterization of its Fréchet derivative via a suitable adjoint system. In Section 3, we give sufficient conditions for the existence and uniqueness of quasi-solutions to **(ISP)**. In Section 4, we validate our theoretical results by some numerical experiments to reconstruct source terms for 1-D and 2-D case. Finally, in Section 5 we give additional comments concerning the theoretical and numerical results obtained in this article.

2 Fréchet differentiability and gradient formula

The differentiability of the misfit functional is central to the design of iterative reconstruction methods. Establishing explicit gradient representations not only ensures theoretical well-posedness of descent algorithms but also provides a concrete path to numerical implementation. We therefore begin by characterizing the gradient of the functional via a suitable adjoint system.

Proposition 2.1. *Consider the assumptions **(H1)** and **(H2)**. Then, the functional $\mathcal{J} : \mathcal{U} \rightarrow \mathbb{R}$ is Fréchet differentiable and its gradient at each $f \in \mathcal{U}$ is given by*

$$\mathcal{J}'(f) = \phi, \quad f \in \mathcal{U}, \quad (2.1)$$

where ϕ is the unique weak solution of the following adjoint system

$$\begin{cases} -\partial_t \phi - \operatorname{div}((a(x) - ib(x))\nabla \phi) - \overline{\vec{r}(x)} \cdot \nabla \phi + (\overline{p(x)} - \overline{\operatorname{div}(\vec{r})(x)})\phi = 0 & \text{in } \Omega \times (0, T), \\ \phi = 0 & \text{on } \partial\Omega \times (0, T), \\ \phi(\cdot, T) = y(\cdot, T; f) - u_T & \text{in } \Omega. \end{cases} \quad (2.2)$$

The adjoint formulation obtained in Proposition 2.1 mirrors the standard duality principles commonly used in PDE-constrained optimization. Its importance lies in reducing the computational cost: instead of computing directional derivatives for each perturbation, the gradient can be evaluated by solving a single adjoint problem, making the approach scalable to high-dimensional discretizations.

Proof. let us consider $f, \delta f \in \mathcal{U}$ such that $f + \delta f \in \mathcal{U}$. Then, our task is to compute the difference

$$\begin{aligned} \delta \mathcal{J}(f) &:= \mathcal{J}(f + \delta f) - \mathcal{J}(f) \\ &= \frac{1}{2} \int_{\Omega} (|y(\cdot, T; f + \delta f) - u_T|^2 - |y(\cdot, T; f) - u_T|^2) dx. \end{aligned}$$

Using the complex identity

$$\frac{1}{2}(|x-z|^2 - |y-z|^2) = \Re[(x-y)\overline{(y-z)}] + \frac{1}{2}|x-y|^2, \quad \forall x, y, z \in \mathbb{C},$$

we have

$$\begin{aligned} \delta\mathcal{J}(f) &= \Re \int_{\Omega} (y(\cdot, T; f + \delta f) - y(\cdot, T; f)) \overline{y(\cdot, T; f) - u_T} \, dx \\ &\quad + \frac{1}{2} \int_{\Omega} |y(\cdot, T; f + \delta f) - y(\cdot, T; f)|^2 \, dx \\ &= -\Re \int_{\Omega} \delta y(\cdot, T; f) \overline{\phi(\cdot, T; f)} \, dx + \frac{1}{2} \int_{\Omega} |\delta y(\cdot, T; f)|^2 \, dx \end{aligned} \quad (2.3)$$

where $\phi(\cdot, \cdot, f)$ is the weak solution of (2.2) (and thanks to Proposition A.2, $\phi(\cdot, T, f) = y(\cdot, T; f) - u_T$ in $L^2(\Omega)$) and δy is the solution of the following *sensitivity problem*

$$\begin{cases} \partial_t \delta y - \operatorname{div}((a(x) + b(x)i)\nabla \delta y) + \vec{r}(x) \cdot \nabla \delta y + p(x)\delta y = \delta f(x, t) & \text{in } \Omega \times (0, T), \\ \delta y = 0 & \text{on } \partial\Omega \times (0, T), \\ \delta y(\cdot, 0) = 0 & \text{in } \Omega. \end{cases} \quad (2.4)$$

Observe that by Proposition A.3, δy is indeed a strong solution of (2.4). Then, integration by parts implies that (2.3) can be written as

$$\delta\mathcal{J}(f) := \Re \int_0^T \int_{\Omega} \delta f \overline{\phi} \, dx \, dt + \frac{1}{2} \int_{\Omega} |\delta y(\cdot, T; f)|^2 \, dx. \quad (2.5)$$

Now, identity (2.5) implies the assertion (2.1). \square

Lemma 2.2. *Under the assumptions **(H1)** and **(H2)**, the Fréchet gradient \mathcal{J}' is Lipschitz continuous in \mathcal{U} , i.e., there exists a constant $M > 0$ such that for all $f, \delta f \in \mathcal{U}$ such that $f + \delta f \in \mathcal{U}$, the following estimate holds:*

$$|\mathcal{J}'(f + \delta f) - \mathcal{J}'(f)| \leq M \|\delta f\|_{L^2(\Omega \times (0, T))}.$$

We point out that the Lipschitz continuity of the gradient guarantees the stability of iterative schemes such as conjugate gradient or quasi-Newton methods, making the result crucial for practical computations. For more details, see Section 4.

The Lipschitz continuity of the gradient ensures that iterative minimization schemes converge under standard step-size rules. In practice, this property prevents instability in the optimization process and justifies the use of line-search or trust-region strategies in the reconstruction algorithm.

Proof. Let us fix $f, \delta f \in \mathcal{U}$ such that $f + \delta f \in \mathcal{U}$. Then, the function $\delta\phi = \delta\phi(\cdot, \cdot, f)$ is the solution of

$$\begin{cases} -\partial_t \delta\phi - \operatorname{div}((a(x) - ib(x))\nabla \phi) - \overline{\vec{r}(x)} \cdot \nabla \phi + (\overline{p(x)} - \overline{\operatorname{div}(\vec{r}(x))})\phi = 0 & \text{in } \Omega \times (0, T), \\ \delta\phi = 0 & \text{on } \partial\Omega \times (0, T), \\ \delta\phi(\cdot, T) = \delta y(\cdot, T; f) & \text{in } \Omega, \end{cases} \quad (2.6)$$

where δy is the solution of (2.2) associated to δf . We remark that, by Proposition A.3, $\delta\phi$ is a strong solution of (2.6). Thus, by Proposition 2.1 we have, for some constant $C > 0$:

$$|\mathcal{J}'(f + \delta f) - \mathcal{J}'(f)| = \|\delta\phi\|_{L^2(\Omega \times (0, T))} \leq C \|\delta y(\cdot, T; f)\|_{L^2(\Omega)} \leq C \|\delta f\|_{L^2(0, T; L^2(\Omega))},$$

where we have used the continuity of the strong solutions applied to δy respect to the data. This proves the assertion of the Lemma 2.2. \square

3 Existence and uniqueness of the solution to (ISP)

Having established the differentiability of the functional, we now turn to the fundamental question of solvability of the (ISP). Existence of quasi-solutions ensures that our variational formulation is mathematically meaningful, while uniqueness conditions determine whether the reconstruction is well-posed or only identifiable up to certain ambiguities.

Before going further, we prove the following

Lemma 3.1. *Let $y_0 \in L^2(\Omega)$ and let y be the weak solution of (1.1) corresponding to f . Then, the solution map $f \mapsto y$ is continuous from $L^2(0, T; L^2(\Omega))$ to $C^0([0, T]; L^2(\Omega)) \cap L^2(0, T; H_0^1(\Omega))$.*

Proof. By density, it is sufficient to consider $y_0 \in H_0^1(\Omega)$. Let δf be a small variation of f such that $f^\delta = f + \delta f \in \mathcal{U}$. Consider $\delta y = y^\delta - y$, where y^δ is the weak solution of (1.1) corresponding to f^δ . Then, by Proposition A.2, we know that

$$\delta y = y(\cdot, \cdot; f^\delta) - y(\cdot, \cdot, f) \in C^0([0, T]; L^2(\Omega)) \cap L^2(0, T; H_0^1(\Omega))$$

and satisfy the following system

$$\begin{cases} \partial_t \delta y - \operatorname{div}((a(x) + b(x)i)\nabla \delta y) + \vec{r}(x) \cdot \nabla \delta y + p(x)\delta y = \delta f(x, t) & \text{in } \Omega \times (0, T), \\ \delta y = 0 & \text{on } \partial\Omega \times (0, T), \\ \delta y(\cdot, 0) = 0 & \text{in } \Omega. \end{cases} \quad (3.1)$$

Therefore, the continuity of the solution δy of (3.1) respect to the data

$$\|\delta y\|_{C^0([0, T]; L^2(\Omega))} + \|\delta y\|_{L^2(0, T; H_0^1(\Omega))} \leq C \|\delta f\|_{L^2(0, T; L^2(\Omega))}$$

proves the assertion of Lemma 3.1. \square

In particular, using the gradient formula (2.1) and the estimates associated to the sensitivity problem (2.4), we will prove the monotonicity of the derivative \mathcal{J}' . In particular, this estimate implies the convexity of the functional \mathcal{J} . Consequently, we have the following existence result:

Corollary 3.2. *The Tikhonov functional \mathcal{J} is continuous and convex on the subset \mathcal{U} . Then, there exists a minimizer $f^* \in \mathcal{F}$ such that*

$$\mathcal{J}(f^*) = \min_{f \in \mathcal{U}} \mathcal{J}(f).$$

Since the strict convexity of \mathcal{J} is characterized by the strict monotonicity of \mathcal{J}' . Besides, after some computations, we have the following sufficient condition for uniqueness.

The convexity of the functional guarantees the existence of minimizers and provides a favorable landscape for optimization. In contrast to non-convex problems, here one avoids the proliferation of spurious local minima, which simplifies the design of reconstruction algorithms.

Lemma 3.3. *If the positivity condition*

$$\int_{\Omega} |\delta y(\cdot, T; f)|^2 dx > 0, \quad \forall f \in \mathcal{V}, \quad (3.2)$$

holds on a closed convex subset $\mathcal{V} \subset \mathcal{U}$, then the problem (ISP) admits at most one solution in \mathcal{V} .

Condition (3.2) reflects the observability of perturbations in the final state. Intuitively, if every non-trivial source produces a distinguishable final profile, uniqueness follows. Such positivity conditions are reminiscent of unique continuation principles in PDEs and are closely tied to the richness of the data.

4 Numerical results

In this section we present the numerical scheme used to recover the complex-valued source factor $q(x, y)$ in the multiplicative model

$$f(x, y, t) = q(x, y) g(t),$$

and report representative results for two-dimensional problems posed on rectangular domains. All computations are performed in `Python` and combine second-order finite differences in space with a Crank–Nicolson (CN) discretization in time for both the forward and adjoint equations. To streamline the exposition and match the implementation, we consider constant coefficients $a > 0$, $b \in \mathbb{R}$, and the model

$$\begin{cases} \partial_t y - (a + i b) \Delta y + p y = f & \text{in } \Omega \times (0, T), \\ y = 0 & \text{on } \partial\Omega \times (0, T), \\ y(\cdot, 0) = y_0 & \text{in } \Omega, \end{cases}$$

with $\Omega = (0, L_{x_1}) \times (0, L_{x_2}) \subset \mathbb{R}^2$. The spatio-temporal modulation g is known and prescribed. In all experiments we enforce homogeneous Dirichlet boundary conditions on u and set $q \equiv 0$ and $g \equiv 0$ on $\partial\Omega$, which implies that f vanishes on the boundary and is supported strictly in the interior.

4.1 Discretization and numerical implementation

We use second-order finite differences on uniform grids

$$x_{1,i} = i \Delta x_1, \quad i = 0, \dots, N_{x_1}, \quad x_{2,j} = j \Delta x_2, \quad j = 0, \dots, N_{x_2},$$

with mesh sizes $\Delta x_1 = L_{x_1}/N_{x_1}$ and $\Delta x_2 = L_{x_2}/N_{x_2}$. Homogeneous Dirichlet data are imposed on $\partial\Omega$; thus the unknowns live on the interior grid

$$\{(x_{1,i}, x_{2,j}) : i = 1, \dots, N_{x_1} - 1, j = 1, \dots, N_{x_2} - 1\}.$$

Let $\Delta_{h_{x_1}} \in \mathbb{R}^{(N_{x_1}-1) \times (N_{x_1}-1)}$ and $\Delta_{h_{x_2}} \in \mathbb{R}^{(N_{x_2}-1) \times (N_{x_2}-1)}$ denote the 1D discrete Dirichlet Laplacians [17],

$$\Delta_{h_{x_1}} = \frac{1}{\Delta x_1^2} \text{tridiag}(1, -2, 1), \quad \Delta_{h_{x_2}} = \frac{1}{\Delta x_2^2} \text{tridiag}(1, -2, 1).$$

With lexicographic ordering, the 2D Laplacian is the Kronecker sum

$$\Delta_h = I_{x_2} \otimes \Delta_{h_{x_1}} + \Delta_{h_{x_2}} \otimes I_{x_1} \in \mathbb{R}^{m \times m}, \quad m = (N_{x_1} - 1)(N_{x_2} - 1), \quad (4.1)$$

where I_{x_1} and I_{x_2} are identity matrices of sizes $N_{x_1} - 1$ and $N_{x_2} - 1$, respectively, and \otimes denotes the Kronecker product.

For the time grid we set $t^n = n \Delta t$, $n = 0, \dots, N_t$, with $\Delta t = T/N_t$. Let $A := (a + i b) \Delta_h + p I_{x_1 \times x_2}$. Following [15], the CN update for the interior degrees of freedom reads

$$M_- y^{n+1} = M_+ y^n + \Delta t f^n, \quad M_\pm = I \pm \frac{\Delta t}{2} A, \quad (4.2)$$

with y^0 given by the samples of y_0 on the interior grid and $I \in \mathbb{C}^{m \times m}$. The forcing is treated by a left-point (rectangle) rule in time, consistent with our choice of quadrature below. Dirichlet

boundary values vanish identically, hence they do not appear in (4.2). The matrix M_- is factorized once (sparse LU) and reused at all time steps.

We approximate space–time integrals using mass–lumped rectangle rules on the interior grid. Define the spatial inner product

$$\langle \xi, \eta \rangle_h := \operatorname{Re}(\xi^* \eta) \Delta x_1 \Delta x_2, \quad \xi, \eta \in \mathbb{C}^m,$$

and the space–time inner product

$$\langle\langle X, Y \rangle\rangle_{h,t} := \sum_{n=0}^{N_t-1} \langle X^n, Y^n \rangle_h \Delta t, \quad \|X\|_{h,t}^2 := \langle\langle X, X \rangle\rangle_{h,t}.$$

Given target samples v_h^n on the interior grid, we consider the *terminal tracking* functional

$$J_h(f) = \frac{1}{2} \langle y^{N_t} - v_h^{N_t}, y^{N_t} - v_h^{N_t} \rangle_h + \frac{\epsilon}{2} \langle\langle f, f \rangle\rangle_{h,t}, \quad \epsilon > 0. \quad (4.3)$$

The discrete adjoint associated with (4.2) and (4.3) is the time–reversed recursion

$$M_-^* \phi^n = M_+^* \phi^{n+1}, \quad n = N_t - 1, \dots, 0, \quad \phi^{N_t} = y^{N_t} - v_h^{N_t}, \quad (4.4)$$

where $(\cdot)^*$ denotes the Hermitian transpose. Since $A = (a + i b) \Delta_h$, we have $A^* = (a - i b) \Delta_h$, and thus $M_\pm^* = I \pm \frac{\Delta t}{2} A^*$. As in the forward solve, M_-^* is factorized once and reused [14].

Remark 4.1. *Since $\Re(a + ib) = a > 0$ and Δ_h is symmetric negative definite under Dirichlet conditions, the operator A is strictly dissipative. The CN scheme is A -stable and second-order accurate for the homogeneous part. With the left-point treatment of the forcing, the method remains unconditionally stable; using a trapezoidal rule for f restores second-order temporal accuracy. In all cases, the spatial discretization is second order.*

By standard Lagrangian arguments (or by differentiating (4.2) directly), the discrete gradient of J_h with respect to the control at time level n is

$$\frac{\partial J_h}{\partial f^n} = \phi^{n+1} + \epsilon f^n \in \mathbb{C}^m, \quad n = 0, \dots, N_t - 1, \quad (4.5)$$

so that $\nabla J_h(f) = (z^{n+1} + \epsilon f^n)_{n=0}^{N_t-1}$.

We minimize J_h using the Polak–Ribi  re+ nonlinear conjugate gradient (NCG) method with Armijo backtracking and an optional L^2 projection onto a closed ball $\{f : \|f\|_{h,t} \leq \rho\}$. This follows the standard framework of PDE-constrained optimization and is summarized in Algorithm 1 [21, 9, 14]. To avoid notational clash with the modulation g , we denote the gradient at iteration k by $r_k := \nabla J_h(f_k)$.

4.2 Numerical experiments

We now present a sequence of test cases designed to assess reconstruction accuracy, robustness to discretization parameters, and sensitivity to noise.

Unless stated otherwise, we set $L_x = L_y = T = 1$, choose $(a, b) = (36 \times 10^{-4}, 15 \times 10^{-4})$ and $p = 0.2 + i 0.1$, employ uniform grids with $(N_x, N_y, N_t) = (100, 100, 70)$, and take the initial condition $u_0(x, y) = \sin(\pi x) \sin(\pi y)$. The Armijo line search uses $c = 10^{-3}$, an initial step α_0 , and a backtracking factor of $1/2$. We restart the Polak–Ribi  re+ method every five iterations or whenever $\langle\langle r_k, d_k \rangle\rangle_{h,t} \geq 0$, where $r_k = \nabla J_h(f_k)$ denotes the gradient.

Algorithm 1 Polak–Ribi  re⁺ NCG with adjoint–based gradients and Armijo line search.

- 1: Choose an initial guess f_0 , set $k = 0$.
- 2: **while** $\|r_k\|_{h,t} \geq \tau$ and $k < k_{\max}$ **do**
- 3: Solve the forward problem (4.2) to obtain $\Psi(f_k)$, then the adjoint (4.4) to obtain $\phi(f_k)$.
- 4: Assemble the gradient $r_k^n = \phi^{n+1}(f_k) + \epsilon f_k^n$ for $n = 0, \dots, N_t - 1$.
- 5: Set the search direction

$$d_k = \begin{cases} -r_k, & \text{if } k = 0 \text{ or } \langle r_k, d_{k-1} \rangle_{h,t} \geq 0, \\ -r_k + \beta_k d_{k-1}, & \text{otherwise,} \end{cases}$$

$$\beta_k = \max \left\{ 0, \frac{\langle r_k - r_{k-1}, r_k \rangle_{h,t}}{\langle r_{k-1}, r_{k-1} \rangle_{h,t} + 10^{-30}} \right\}.$$

- 6: Perform Armijo backtracking to find $\alpha > 0$ such that

$$J_h(f_k + \alpha d_k) \leq J_h(f_k) + c \alpha \langle r_k, d_k \rangle_{h,t}, \quad c \in (0, 1).$$

- 7: Update $f_{k+1} = f_k + \alpha d_k$ and, if needed, project onto the L^2 ball; set $k \leftarrow k + 1$.
- 8: **end while**

4.2.1 Example 1 (Smooth real-valued source)

Our first example considers a smooth real-valued source, serving as a baseline for algorithm verification.

As a benchmark, we consider the smooth real-valued source

$$q(x, y) = \sin(2\pi x) \sin(2\pi y).$$

Here $\Psi(f)$ denotes the forward solution evaluated at the final time $t = T$, and u_T the measured final state. All error metrics below are relative discrete L^2 errors, using the norm induced by $\langle \cdot, \cdot \rangle_h$.

Table 1 reports the performance as the stopping tolerance τ varies for fixed regularization $\epsilon = 10^{-5}$. As τ decreases, the iteration count increases and both the data misfit $\|\Psi(f) - u_T\|_h / \|u_T\|_h$ and the source error $\|q_{\text{rec}} - q\|_h / \|q\|_h$ decrease, as expected for a tighter termination criterion.

Table 1: Effect of the stopping tolerance with $\epsilon = 10^{-5}$.

τ	iterations	$\ \Psi(f) - u_T\ _h^2$	$\ q_{\text{rec}} - q\ _h^2$
		$\ \Psi(f) - u_T\ _h^2 / \ u_T\ _h^2$	$\ q_{\text{rec}} - q\ _h^2 / \ q\ _h^2$
10^{-3}	36	1.2577×10^{-3}	1.9513×10^{-3}
10^{-4}	49	1.2415×10^{-4}	1.9262×10^{-4}
10^{-5}	62	2.0756×10^{-5}	3.2202×10^{-5}
10^{-6}	76	8.2193×10^{-6}	1.2751×10^{-5}

Table 2 shows that the algorithm is robust with respect to mesh and time refinements: the iteration counts remain essentially unchanged and the relative errors are stable across (N_x, N_y, N_t) .

Table 3 illustrates the classical behavior of Tikhonov regularization as ϵ varies (with fixed $\tau = 10^{-5}$). In the noise-free setting, smaller ϵ reduces the data misfit and reconstruction error, while larger ϵ enforces stronger smoothing at the expense of higher bias.

Table 2: Mesh and time sensitivity for $\epsilon = 10^{-5}$ and $\tau = 10^{-5}$.

(N_x, N_y, N_t)	iterations	$\frac{\ \Psi(f) - u_T\ _h^2}{\ u_T\ _h^2}$	$\frac{\ q_{\text{rec}} - q\ _h^2}{\ q\ _h^2}$
(35, 35, 70)	63	5.6624×10^{-6}	8.7835×10^{-6}
(50, 50, 70)	63	5.0117×10^{-6}	7.7749×10^{-6}
(100, 100, 70)	62	2.0756×10^{-5}	3.2202×10^{-5}
(100, 100, 150)	62	2.0173×10^{-5}	3.1298×10^{-5}

Table 3: Effect of ϵ with $(N_x, N_y, N_t) = (100, 100, 70)$ and $\tau = 10^{-5}$.

ϵ	iterations	$\frac{\ \Psi(f) - u_T\ _h^2}{\ u_T\ _h^2}$	$\frac{\ q_{\text{rec}} - q\ _h^2}{\ q\ _h^2}$
10^{-3}	63	6.8617×10^{-4}	1.0646×10^{-3}
10^{-4}	62	8.3959×10^{-5}	1.3026×10^{-4}
10^{-5}	62	2.0756×10^{-5}	3.2202×10^{-5}
10^{-6}	62	1.4436×10^{-5}	2.2396×10^{-5}

Figures 1–2 compare the reconstructed and measured final states, displaying real and imaginary parts of $\Psi(f)$ and u_T . The close agreement is consistent with the value of the tracking functional (cf. (4.3)).

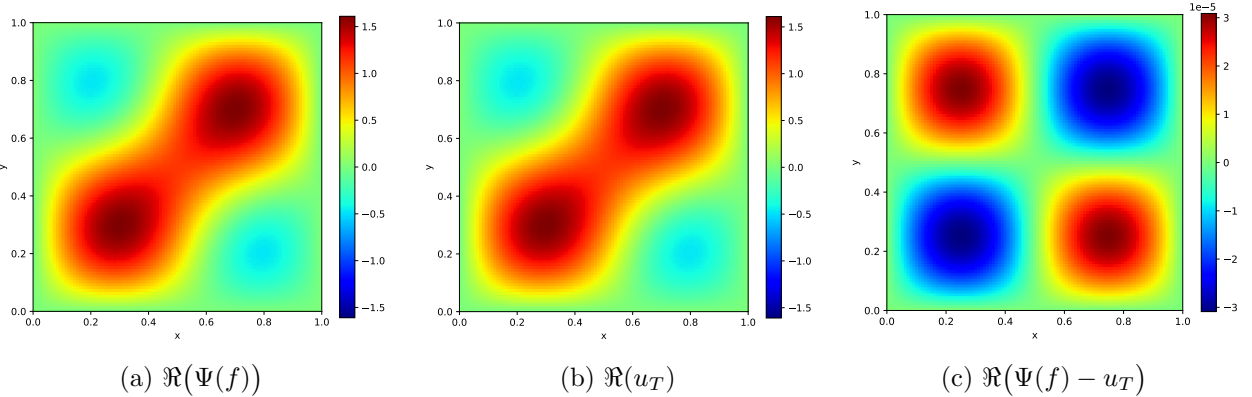


Figure 1: Final-time comparison: real part. Parameters $(N_x, N_y, N_t) = (100, 100, 70)$, $\tau = 10^{-5}$, $\epsilon = 10^{-5}$.

Figures 3–4 display the recovered source q_{rec} and the true source q . The reconstruction closely matches the ground truth; the residual plots confirm that the remaining discrepancies are small and spatially localized.

4.2.2 Example 2 (Localized imaginary Gaussian source)

We next examine a localized imaginary source to test spatial selectivity and robustness of the inversion.

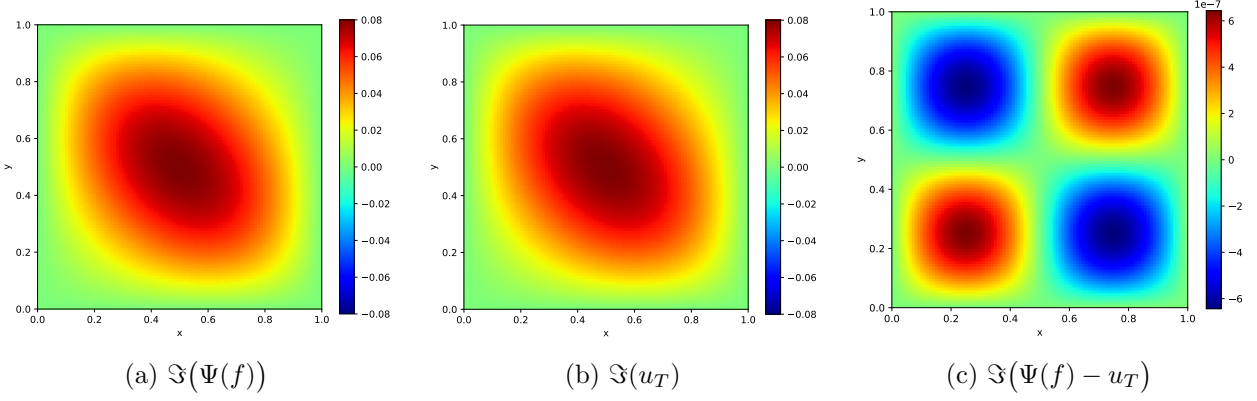


Figure 2: Final-time comparison: imaginary part. Parameters $(N_x, N_y, N_t) = (100, 100, 70)$, $\tau = 10^{-5}$, $\epsilon = 10^{-5}$.

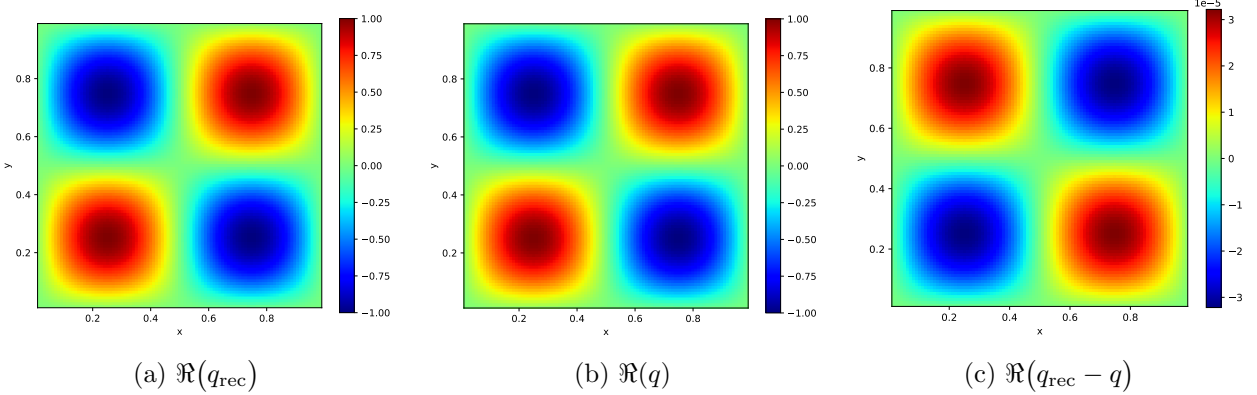


Figure 3: Recovered vs. true source (real part). Parameters $(N_x, N_y, N_t) = (100, 100, 70)$, $\tau = 10^{-5}$, $\epsilon = 10^{-5}$.

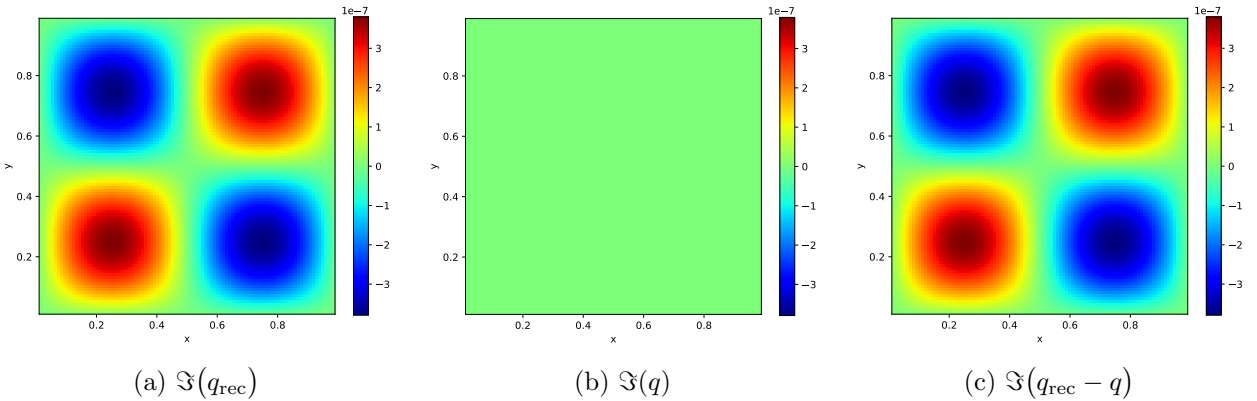


Figure 4: Recovered vs. true source (imaginary part). Parameters $(N_x, N_y, N_t) = (100, 100, 70)$, $\tau = 10^{-5}$, $\epsilon = 10^{-5}$.

In this example we consider a purely imaginary, Gaussian-modulated source,

$$q(x, y) = i \exp\left(-\frac{(x - \frac{1}{2})^2 + (y - \frac{1}{2})^2}{2\sigma^2}\right) \sin(\pi x) \sin(\pi y), \quad \sigma = 0.12, \quad (4.6)$$

which is spatially localized around the domain center.

Figures 5–6 compare the reconstructed and measured final states, showing the real and imaginary parts of $\Psi(f)$ and u_T . The plots indicate excellent agreement; the relative (discrete) L^2 data misfit is

$$\frac{\|\Psi(f) - u_T\|_h^2}{\|u_T\|_h^2} = 4.2617 \times 10^{-5}.$$

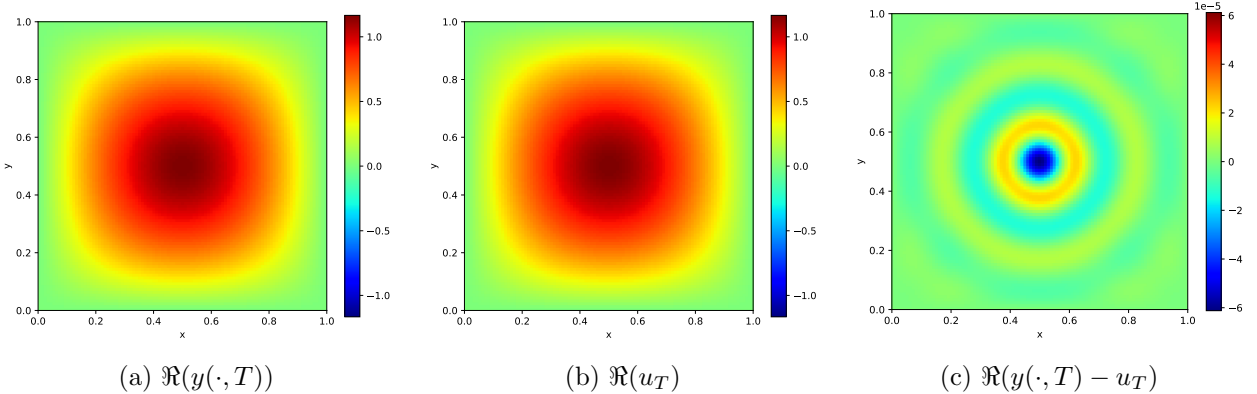


Figure 5: Final-time comparison: real part. Parameters $(N_x, N_y, N_t) = (100, 100, 70)$, $\tau = 10^{-5}$, $\varepsilon = 10^{-5}$.

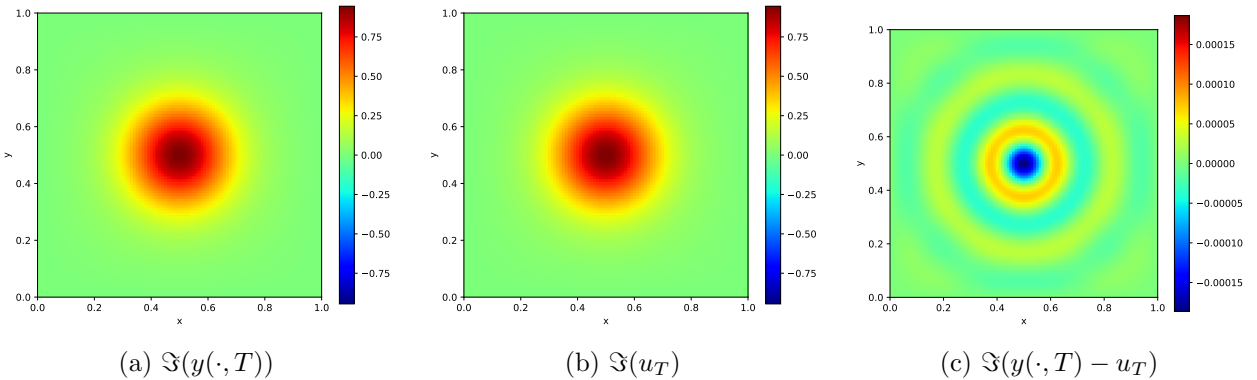


Figure 6: Final-time comparison: imaginary part. Parameters $(N_x, N_y, N_t) = (100, 100, 70)$, $\tau = 10^{-5}$, $\varepsilon = 10^{-5}$.

Figures 7–8 display the recovered source q_{rec} alongside the ground truth q from (4.6). The reconstruction is highly accurate; the residuals are small and spatially localized. The relative (discrete) L^2 reconstruction error is

$$\frac{\|q_{\text{rec}} - q\|_h^2}{\|q\|_h^2} = 4.3644 \times 10^{-4}.$$

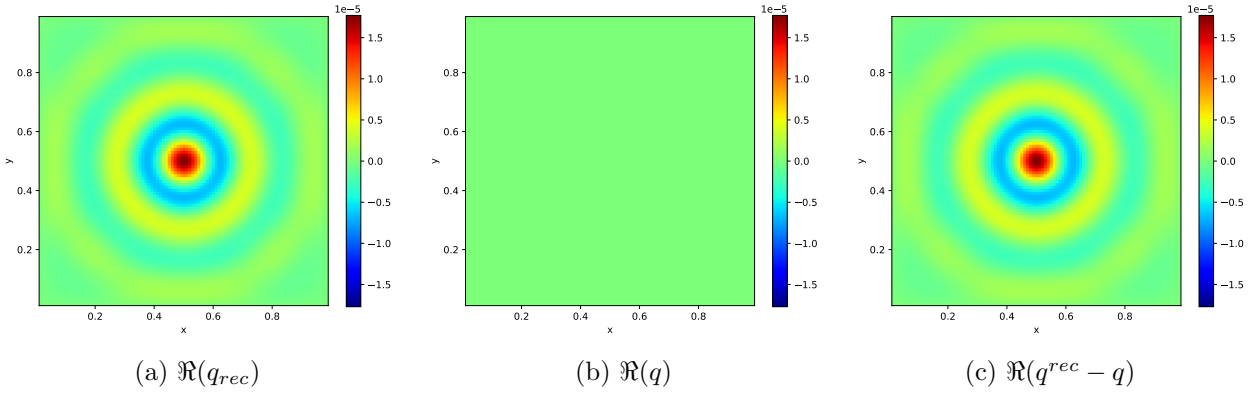


Figure 7: Recovered vs. true source (real part). Parameters $(N_x, N_y, N_t) = (100, 100, 70)$, $\tau = 10^{-5}$, $\varepsilon = 10^{-5}$.

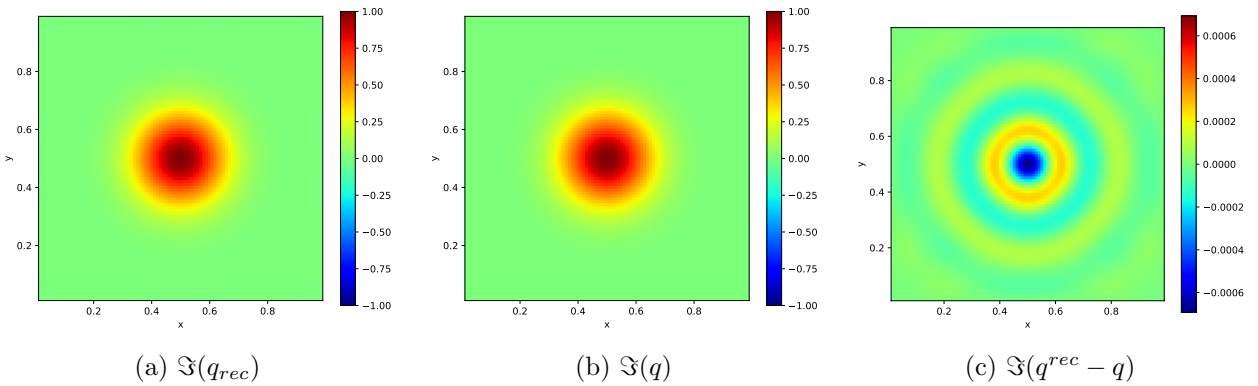


Figure 8: Recovered vs. true source (imaginary part). Parameters $(N_x, N_y, N_t) = (100, 100, 70)$, $\tau = 10^{-5}$, $\varepsilon = 10^{-5}$.

4.2.3 Example 3 (Complex source with mixed frequencies)

This example explores a complex source that combines distinct spatial frequencies in its real and imaginary parts. We consider

$$q(x, y) = \sin(2\pi x) \sin(2\pi y) + i 0.7 \sin(3\pi x) \sin(2\pi y), \quad (x, y) \in (0, 1)^2. \quad (4.7)$$

Figures 9–10 compare the reconstructed and measured final states, displaying the real and imaginary parts of $\Psi(f)$ and u_T . The agreement is excellent; the relative (discrete) L^2 data misfit equals

$$\frac{\|\Psi(f) - u_T\|_h^2}{\|u_T\|_h^2} = 1.9803 \times 10^{-5}.$$

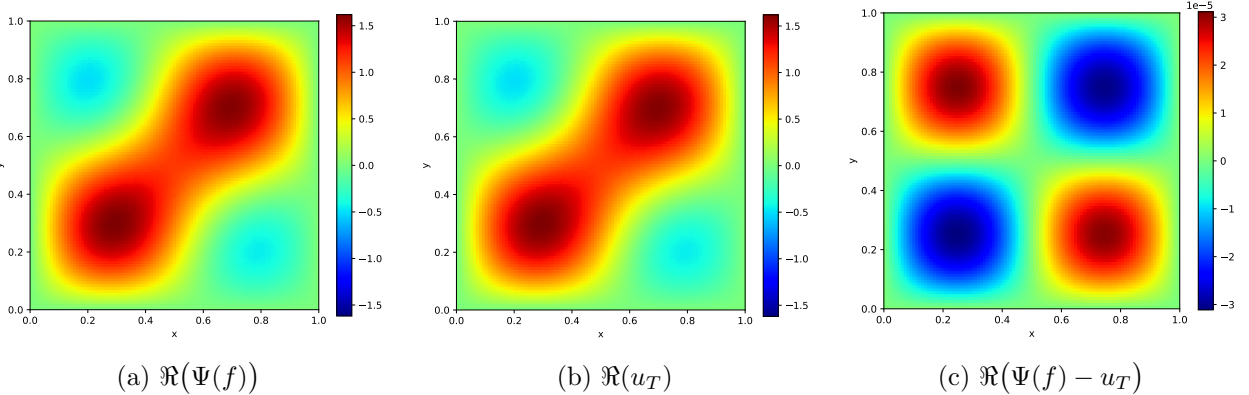


Figure 9: Final-time comparison: real part. Parameters $(N_x, N_y, N_t) = (100, 100, 70)$, $\tau = 10^{-5}$, $\varepsilon = 10^{-5}$.

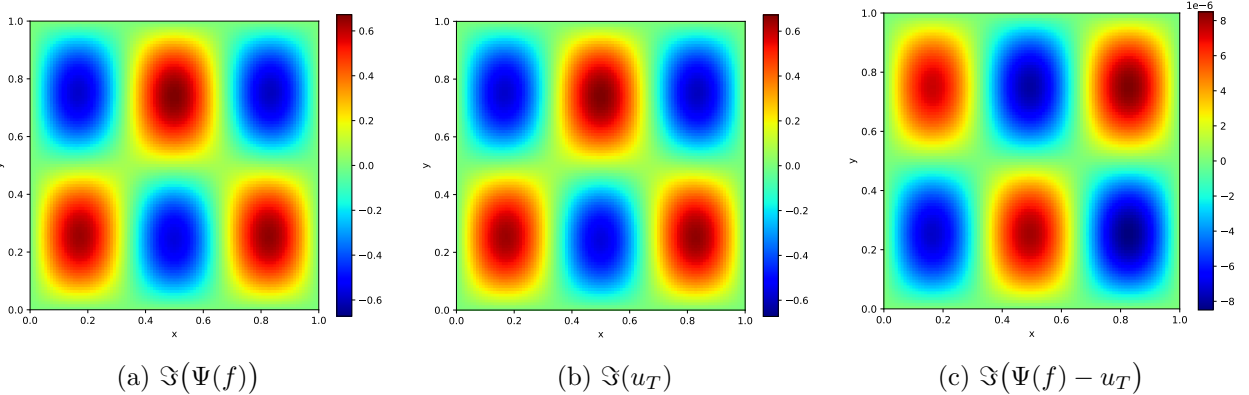


Figure 10: Final-time comparison: imaginary part. Parameters $(N_x, N_y, N_t) = (100, 100, 70)$, $\tau = 10^{-5}$, $\varepsilon = 10^{-5}$.

Figures 11–12 display the recovered source q_{rec} alongside the ground truth q from (4.7). The reconstruction is highly accurate; residuals are small and spatially localized. The relative (discrete) L^2 reconstruction error is

$$\frac{\|q_{\text{rec}} - q\|_h^2}{\|q\|_h^2} = 2.7399 \times 10^{-5}.$$

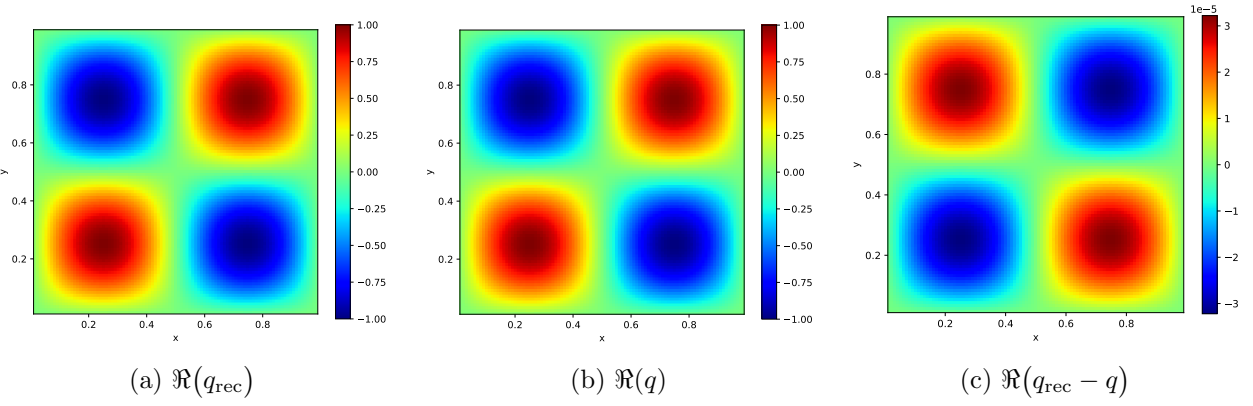


Figure 11: Recovered vs. true source (real part). Parameters $(N_x, N_y, N_t) = (100, 100, 70)$, $\tau = 10^{-5}$, $\varepsilon = 10^{-5}$.

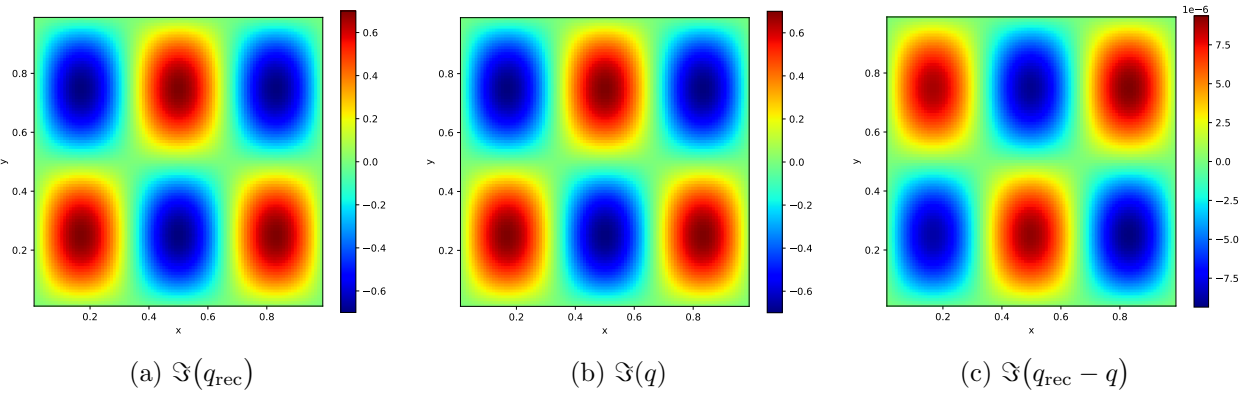


Figure 12: Recovered vs. true source (imaginary part). Parameters $(N_x, N_y, N_t) = (100, 100, 70)$, $\tau = 10^{-5}$, $\varepsilon = 10^{-5}$.

To assess robustness, we corrupt the exact final state $u_T = u(\cdot, T)$ with circularly symmetric complex Gaussian noise at a prescribed relative level $\delta \in (0, 1)$. Let $\xi = \xi_1 + i \xi_2$, where ξ_1, ξ_2 have i.i.d. standard normal entries, and define

$$u_T^\delta = u_T + \eta^\delta, \quad \eta^\delta = \delta \frac{\|u_T\|_h}{\|\xi\|_h} \xi, \quad (4.8)$$

so that $\|u_T^\delta - u_T\|_h / \|u_T\|_h = \delta$. In reconstructions with noise we replace the target $v_h^{N_t}$ in (4.3) by u_T^δ ; the algorithm is otherwise unchanged. Misfit values are reported in the same discrete norm $\|\cdot\|_h$.

Table 4: Noisy-data reconstructions for $\varepsilon = 10^{-5}$ and $\tau = 10^{-5}$. The misfit is computed with u_T^δ in place of u_T (for $\delta = 0$, $u_T^\delta = u_T$).

δ	iterations	$\frac{\ \Psi(f) - u_T^\delta\ _h^2}{\ u_T^\delta\ _h^2}$	$\frac{\ q_{\text{rec}} - q\ _h^2}{\ q\ _h^2}$
		$\ \Psi(f) - u_T^\delta\ _h^2$	$\ q_{\text{rec}} - q\ _h^2$
0	62	1.9803×10^{-5}	2.7399×10^{-5}
1×10^{-3}	443	8.5539×10^{-4}	1.8720×10^{-2}
5×10^{-3}	8764	1.4810×10^{-3}	7.3337×10^{-1}

In the presence of noise, the Tikhonov parameter ε must balance bias and variance. For instance, for $\delta = 10^{-3}$ we also considered $\varepsilon = 10^{-3}$; in that case, after 109 iterations the relative source error is

$$\frac{\|q_{\text{rec}} - q\|_h^2}{\|q\|_h^2} = 5.1450 \times 10^{-3}.$$

4.2.4 Example 4 (Space–time forcing)

In this example we consider a space–time forcing of the form

$$f(x, y, t) = i \exp\left(-\frac{((x - \frac{1}{2})^2 + (y - \frac{1}{2})^2) t}{2\sigma^2}\right) \sin(\pi x) \sin(\pi y), \quad \sigma = 0.12. \quad (4.9)$$

Figures 13–14 compare the reconstructed and measured final states, showing the real and imaginary parts of $\Psi(f)$ and u_T . The agreement is excellent; the relative (discrete) L^2 data misfit is

$$\frac{\|\Psi(f) - u_T\|_h^2}{\|u_T\|_h^2} = 1.0473 \times 10^{-5}.$$

Figures 15–16 display the recovered forcing f_{rec} and the ground-truth f from (4.9) at the final time slice $t = T$. The reconstruction of the state is essentially exact, whereas the recovered forcing exhibits a moderate discrepancy. The relative (discrete) space–time error is

$$\frac{\|f_{\text{rec}} - f\|_{h,t}^2}{\|f\|_{h,t}^2} = 3.1720 \times 10^{-1}.$$

Remark 4.2 (Identifiability with a single terminal observation). *In space–time source inversion from a single time slice, many different forcings f can produce nearly identical terminal states $u(\cdot, T)$. Consequently, while $\Psi(f)$ matches u_T to high accuracy, the recovery of f is only approximate in the space–time norm. Incorporating additional data (e.g., multi-time observations) or temporal regularization can improve identifiability and reduce the reconstruction error.*

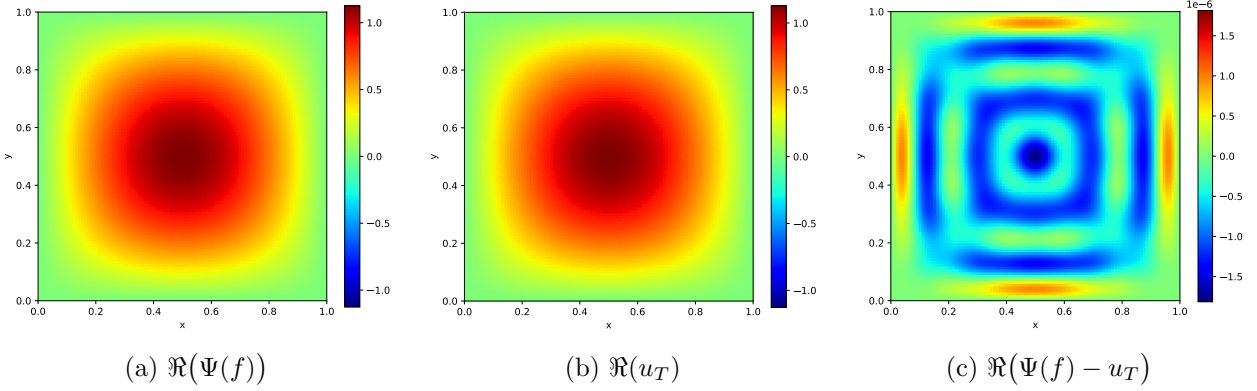


Figure 13: Final-time comparison: real part. Parameters $(N_x, N_y, N_t) = (100, 100, 70)$, $\tau = 10^{-5}$, $\varepsilon = 10^{-5}$.

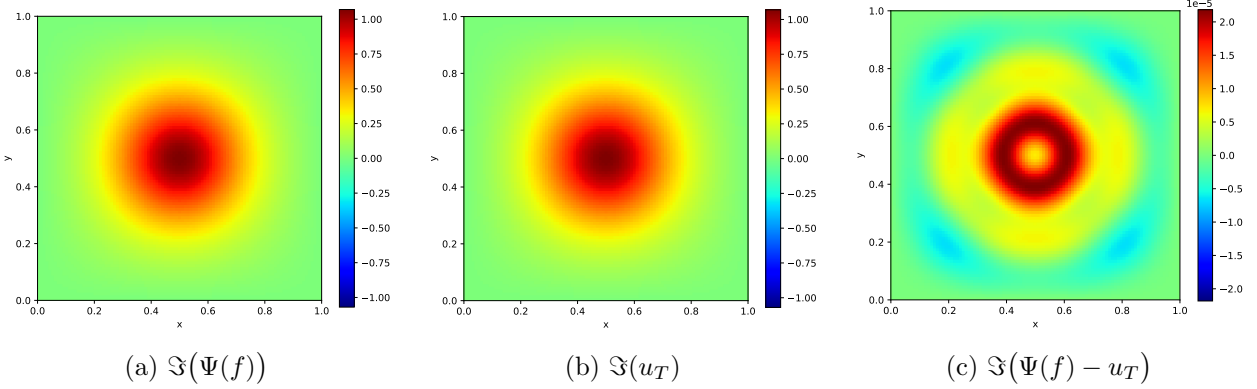


Figure 14: Final-time comparison: imaginary part. Parameters $(N_x, N_y, N_t) = (100, 100, 70)$, $\tau = 10^{-5}$, $\varepsilon = 10^{-5}$.

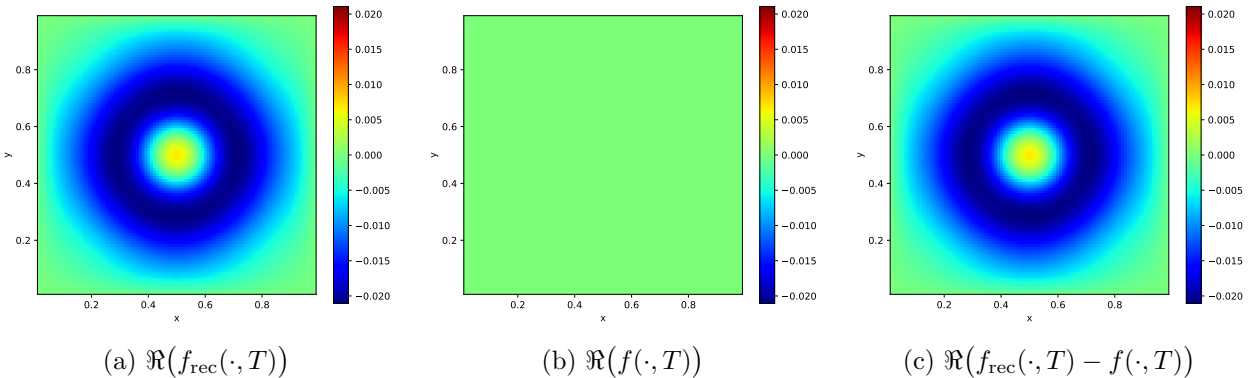


Figure 15: Recovered vs. true forcing at $t = T$ (real part). Parameters $(N_x, N_y, N_t) = (100, 100, 70)$, $\tau = 10^{-5}$, $\varepsilon = 10^{-5}$.

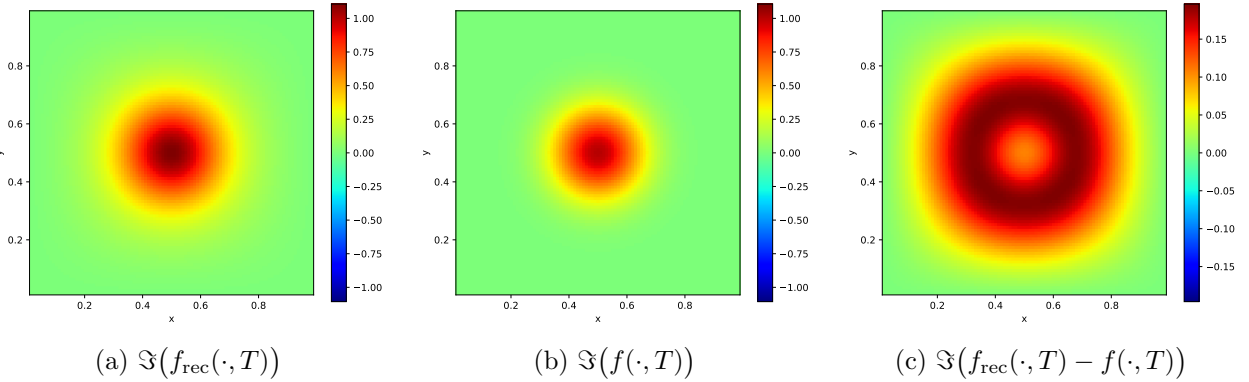


Figure 16: Recovered vs. true forcing at $t = T$ (imaginary part). Parameters $(N_x, N_y, N_t) = (100, 100, 70)$, $\tau = 10^{-5}$, $\varepsilon = 10^{-5}$.

5 Conclusions and open problems

In this article, we have investigated an inverse source problem for the Ginzburg-Landau equation, aiming to recover an unknown space-time dependent forcing term from final-time observations. Within a weak-solution framework, we formulated the reconstruction task as the minimization of a Tikhonov-regularized functional and derived an explicit gradient expression through an adjoint system.

We proved the Lipschitz continuity of this gradient, ensuring both the theoretical stability of the optimization procedure and the convergence of gradient-based numerical schemes. Furthermore, we established existence and uniqueness results for quasi-solutions, thus providing a rigorous variational foundation for the inverse identification process.

From the numerical point of view, we implemented an adjoint-based optimization algorithm relying on Crank-Nicolson time discretization and second-order finite differences in space. The resulting method was tested on several two-dimensional examples, confirming its ability to accurately reconstruct complex-valued sources even under moderate noise perturbations.

The numerical evidence aligns with the analytical predictions: the regularized functional exhibits a well-behaved convex structure, and the reconstructed source converges toward the exact ones as the tolerance and regularization parameters are refined.

Beyond these specific findings, our study highlights the broader significance of the Ginzburg-Landau (GL) equation as a model for dissipative-dispersive dynamics. Because the GL framework appears in contexts as diverse as nonlinear optics, hydrodynamic instabilities, and chemical pattern formation, advances in its inverse analysis have wide interdisciplinary implications. The techniques developed here therefore provide a foundation not only for the reconstruction of hidden excitations in amplitude-equation models but also for related PDE-constrained optimization and control problems.

At the same time, several important directions remain open and deserve future exploration:

1. **Nonlinear extensions.** Extending the present analysis to the cubic and cubic-quintic GL equations would bring the inverse-problem framework closer to realistic physical models. The main difficulty lies in handling the nonlinear coupling between amplitude and phase, which may lead to multiple local minima and non-convex optimization landscapes.
2. **Quantitative stability estimates.** While the current work ensures Lipschitz continuity of the gradient, obtaining explicit conditional stability bounds for the reconstructed source (possibly of logarithmic or Hölder type) remains an open theoretical challenge.

3. **Alternative regularization strategies.** Incorporating sparsity-promoting, adaptive, or data-driven regularization (e.g., L^1 or total-variation penalties) bounds for the reconstructed source (e.g., possibly of logarithmic or Hölder type) remains an open theoretical challenge.
4. **Numerical and computational challenges.** Large-scale simulations of the GL equation involve stiff, highly oscillatory dynamics due to the coexistence of diffusion and dispersion. Developing structure-preserving or phase-accurate discretizations (such as exponential integrators or operator-splitting schemes) may significantly enhance the stability and efficiency of inversion algorithms.
5. **Integration with machine-learning surrogates.** Combining adjoint-based inversion with neural surrogates offers a promising path to accelerate computations and to infer effective source representations in nonlinear or high-dimensional regimes.

In summary, this article provides a rigorous and computationally validated framework for the inverse identification of source terms in the Ginzburg-Landau equation. By unifying analytical well-posedness, adjoint-based gradient characterization, and efficient numerical implementation, it establishes a solid platform for further research on dissipative-dispersive inverse problems.

Addressing the open challenges listed above will deepen the mathematical understanding of these systems and foster new connections between (nonlinear) inverse problems and modern computational approaches.

Acknowledgments

R. Morales has received funding from the European Research Council (ERC) under the European Union's Horizon 2030 research and innovation programme (grant agreement NO: 101096251-CoDeFeL). J. Ramirez was partially supported by Centro de Modelamiento Matemático (CMM) Grant ANID ACE210010 and Basal FB210005.

References

- [1] AKHMEDIEV, N., AND ANKIEWICZ, A. *Dissipative Solitons*. Springer Tracts in Modern Physics. Springer, 2005.
- [2] ARANSON, I. S., AND KRAMER, L. The world of the complex Ginzburg–Landau equation. *Reviews of Modern Physics* 74, 1 (2002), 99–143.
- [3] BARTUCELLI, M., CONSTANTIN, P., DOERING, C. R., GIBBON, J. D., AND GISSELFÄLT, M. On the possibility of soft and hard turbulence in the complex Ginzburg-Landau equation. *Physica D: Nonlinear Phenomena* 44, 3 (1990), 421–444.
- [4] BORZI, A., GROSSAUER, H., AND SCHERZER, O. Analysis of iterative methods for solving a ginzburg-landau equation. *International Journal of Computer Vision* 64, 2 (2005), 203–219.
- [5] CARREÑO, N., MERCADO, A., AND MORALES, R. Local null controllability of a cubic Ginzburg–Landau equation with dynamic boundary conditions. *Journal of Evolution Equations* 25, 3 (2025), 62.
- [6] CHEN, Z., AND HOFFMANN, K.-H. Numerical solutions of an optimal control problem governed by a Ginzburg-Landau model in superconductivity. *Numerical functional analysis and optimization* 19, 7-8 (1998), 737–757.

- [7] CHORFI, S.-E., HASANOV, A., AND MORALES, R. Identification of source terms in the schrödinger equation with dynamic boundary conditions from final data. *Zeitschrift für angewandte Mathematik und Physik* 76, 3 (2025), 127.
- [8] CROSS, M. C., AND HOHENBERG, P. C. Pattern formation outside of equilibrium. *Reviews of Modern Physics* 65, 3 (1993), 851–1112.
- [9] DAI, Y. H., AND YUAN, Y. A nonlinear conjugate gradient method with a strong global convergence property. *SIAM J. Optim.* 10, 1 (1999), 177–182.
- [10] FURSIKOV, A. V., AND IMANUVILOV, O. Y. Controllability of evolution equations. *Lecture Notes Series* 34 (1996). Carleman estimates and control for parabolic PDEs.
- [11] GARCIA, G. C., OSSES, A., AND TAPIA, M. A heat source reconstruction formula from single internal measurements using a family of null controls. *Journal of Inverse and Ill-Posed Problems* 21, 6 (2013), 755–779.
- [12] HASANOĞLU, A. H., AND ROMANOV, V. G. *Introduction to inverse problems for differential equations*. Springer, 2021.
- [13] HASANOV, A. Simultaneous determination of source terms in a linear parabolic problem from the final overdetermination: weak solution approach. *Journal of Mathematical Analysis and Applications* 330, 2 (2007), 766–779.
- [14] HINZE, M., PINNAU, R., ULRICH, M., AND ULRICH, S. *Optimization with PDE constraints*, vol. 23 of *Mathematical Modelling: Theory and Applications*. Springer, New York, 2009.
- [15] HUNSDORFER, W., AND VERWER, J. *Numerical solution of time-dependent advection-diffusion-reaction equations*, vol. 33 of *Springer Series in Computational Mathematics*. Springer-Verlag, Berlin, 2003.
- [16] JUNGE, L., AND PARLITZ, U. Synchronization and control of coupled ginzburg-landau equations using local coupling. *Physical Review E* 61, 4 (2000), 3736.
- [17] LEVEQUE, R. J. *Finite difference methods for ordinary and partial differential equations*. Society for Industrial and Applied Mathematics (SIAM), Philadelphia, PA, 2007. Steady-state and time-dependent problems.
- [18] LEVERMORE, C. D., AND OLIVER, M. The complex Ginzburg-Landau equation as a model problem. *Lectures in applied Mathematics* 31 (1996), 141–190.
- [19] MIELKE, A. The Ginzburg-Landau equation in its role as a modulation equation. In *Handbook of dynamical systems*, vol. 2. Elsevier, 2002, pp. 759–834.
- [20] NEWELL, A. C., AND WHITEHEAD, J. A. Finite bandwidth, finite amplitude convection. *Journal of Fluid Mechanics* 38 (1969), 279–303.
- [21] NOCEDAL, J., AND WRIGHT, S. J. *Numerical optimization*, second ed. Springer Series in Operations Research and Financial Engineering. Springer, New York, 2006.
- [22] SANTOS, M. C., AND TANAKA, T. Y. An insensitizing control problem for the ginzburg–landau equation. *Journal of Optimization Theory and Applications* 183, 2 (2019), 440–470.

[23] SOTO-CRESPO, J. M., AKHMEDIEV, N. N., AND AFANASJEV, V. V. Pulsating, exploding and chaotic solitons in the cubic-quintic complex Ginzburg-Landau equation. *Physical Review Letters* 78, 21 (1997), 4047–4050.

A Existence and uniqueness results for the linearized GL equation

This appendix provides standard existence and regularity results for the linearized Ginzburg-Landau equation. These results justify the analytical framework adopted in the main text and ensure the well-posedness of both forward and adjoint systems.

For completeness, we recall the main existence and uniqueness results for the linearized GL equation, which provide the analytical backbone for the weak and strong solution frameworks used throughout this paper. These results, while classical in the parabolic PDE literature, are here adapted to the complex-valued GL operator with mixed dissipative-dispersive terms.

Let $\Omega \subset \mathbb{R}^N$ be a bounded domain with Lipschitz boundary $\partial\Omega$ and $T > 0$. Consider the problem

$$\begin{cases} \partial_t v - \operatorname{div}((\alpha(x) + \beta(x)i)\nabla v) + \vec{\sigma}(x) \cdot \nabla v + p(x)v = h(x, t) & \text{in } \Omega \times (0, T), \\ v = 0 & \text{on } \partial\Omega \times (0, T), \\ v(\cdot, 0) = v_0 & \text{in } \Omega. \end{cases} \quad (\text{A.1})$$

Definition A.1. *We say that*

- *v is a weak solution of (A.1) if v has the following regularity*

$$v \in L^2(0, T; H_0^1(\Omega)), \quad \partial_t v \in L^2(0, T; H^{-1}(\Omega)), \quad (\text{A.2})$$

and if for every test function $\varphi \in H_0^1(\Omega)$ and almost every $t \in (0, T)$, we have

$$\frac{d}{dt} \langle v(t), \varphi \rangle_{H^{-1}, H_0^1} + \int_{\Omega} (\alpha(x) + \beta(x)i)\nabla v(t) \cdot \nabla \bar{\varphi} dx + \int_{\Omega} py\bar{\varphi} dx = \int_{\Omega} h(t)\bar{\varphi} dx \quad (\text{A.3})$$

with initial condition

$$v(\cdot, 0) = v_0. \quad (\text{A.4})$$

- *v is a strong solution of (A.1) if $v \in L^2(0, T; H_0^1(\Omega) \cap H^2(\Omega))$ and it satisfies*

$$\partial_t v - \operatorname{div}((\alpha(x) + \beta(x)i)\nabla v) + \vec{\sigma}(x) \cdot \nabla v + pv = h \text{ in } L^2(0, T; L^2(\Omega)),$$

and the initial condition (A.4).

Concerning the existence of weak solutions for the problem (A.1), we have the following result:

Proposition A.2. *Assume that the coefficients α, β and q satisfy*

$$\alpha, \beta \in L^{\infty}(\Omega; \mathbb{R}), \quad \alpha(x) \geq \alpha_0 > 0 \text{ almost everywhere in } \Omega, \quad (\text{A.5})$$

and

$$\vec{\sigma} \in [L^{\infty}(\Omega)]^N \text{ and } q \in L^{\infty}(\Omega) \quad (\text{A.6})$$

Moreover, let $v_0 \in L^2(\Omega)$ and $h \in L^2(0, T; H^{-1}(\Omega))$. Then, there exists a unique weak solution

$$v \in L^2(0, T; H_0^1(\Omega)) \cap C^0([0, T]; L^2(\Omega)), \quad \partial_t v \in L^2(0, T; H^{-1}(\Omega)), \quad (\text{A.7})$$

satisfying the variational formulation (A.3). Moreover, there exists a constant $C > 0$ depending on α_0 , $\|\alpha\|_{L^\infty}$, $\|\vec{\sigma}\|_{L^\infty}$ and $\|q\|_{L^\infty}$, Ω and T such that

$$\max_{t \in [0, T]} \|v(t)\|_{L^2(\Omega)}^2 + \int_0^T \|\nabla v(t)\|_{L^2(\Omega)}^2 dt \leq C \left(\|v_0\|_{L^2(\Omega)}^2 + \|g\|_{L^2(0, T; H^{-1}(\Omega))}^2 \right). \quad (\text{A.8})$$

The existence of weak solutions under mild assumptions on the coefficients ensures that the variational framework is robust. In particular, it shows that the adjoint system, central to the gradient formula, is always well-posed.

Proof. We divide the proof into several steps:

- *Step 1: Galerkin basis and finite dimensional problems.* Let $\{w_k\}_{k \geq 1}$ be an orthonormal basis of $L^2(\Omega)$ consisting of functions in $H_0^1(\Omega)$ (for instance we can consider the eigenfunctions of the (complex) Dirichlet Laplacian). For each $m \in \mathbb{N}$, define the finite-dimensional space $V_m := \text{span}\{w_1, \dots, w_m\}$ and the L^2 -orthogonal projection $P_m : L^2 \rightarrow V_m$.

We look for y_m of the form

$$v_m(t) = \sum_{k=1}^m c_k^{(m)}(t) w_k,$$

with coefficients determined by the finite-dimensional system

$$\begin{aligned} & (\partial_t y_m, \varphi)_{L^2(\Omega)} + \int_{\Omega} (\alpha + \beta i) \nabla v_m(t) \cdot \nabla \bar{\varphi} dx + \int_{\Omega} (\vec{\sigma} \cdot \nabla v_m + p v_m) \bar{\varphi} dx \\ &= \langle g(t), \varphi \rangle_{H^{-1}, H_0^1}, \quad \forall \varphi \in V_m, \end{aligned} \quad (\text{A.9})$$

with initial condition $v_m(0) = P_m v_0$. Notice that (A.9) defines a linear ODE system for the coefficients $\{c_k^{(m)}\}$. Hence, by classical results, there exists a unique maximal C^1 solution on $[0, T]$.

- *Step 2: A priori uniform energy estimate in m .* Now, we choose $\varphi = v_m(t)$ in (A.9) and take the real part. Moreover, taking into account that

$$\Re((\alpha + \beta i) \nabla v \cdot \nabla \bar{v}) = a |\nabla v|^2,$$

and

$$\Re \int_{\Omega} (\vec{\sigma} \cdot \nabla v_m(t) \bar{v}_m + p |v_m|^2) dx \geq -\|\vec{\sigma}\|_{L^\infty} \cdot \|\nabla v_m\|_{L^2} \cdot \|v_m\|_{L^2} - \|q\|_{L^\infty} \|v_m\|_{L^2}^2,$$

a.e. $t \in (0, T)$, and using Young's inequality we have

$$\begin{aligned} & \frac{1}{2} \frac{d}{dt} \|v_m\|_{L^2}^2 + \alpha_0 \|\nabla v_m\|_{L^2}^2 \\ & \leq \frac{\alpha_0}{2} \|\nabla v_m\|_{L^2}^2 + \left(\frac{\|\vec{\sigma}\|_{L^\infty}}{\alpha_0} + \|p\|_{L^\infty} \right) \|v_m\|_{L^2}^2 + \frac{1}{\alpha_0} \|h\|_{H^{-1}}^2. \end{aligned} \quad (\text{A.10})$$

Equivalently, this means that

$$\frac{d}{dt} \|v_m\|_{L^2}^2 + \alpha_0 \|\nabla v_m\|_{L^2}^2 \leq \gamma_1 \|v_m\|_{L^2}^2 + \frac{2}{\alpha_0} \|h\|_{H^{-1}}^2, \quad (\text{A.11})$$

where $\gamma := 2 \left(\frac{\|\vec{\sigma}\|_{L^\infty}^2}{\alpha_0} + \|p\|_{L^\infty} \right)$. Now, by Grönwall's inequality, we deduce that

$$\|v_m(t)\|_{L^2}^2 \leq e^{\gamma_1 t} \left(\|v_0\|_{L^2}^2 + \frac{2}{\alpha_0} \int_0^t e^{\gamma_1 s} \|h(s)\|_{H^{-1}}^2 ds \right), \quad \forall t \in [0, T]. \quad (\text{A.12})$$

In particular, by (A.12), the sequence (v_m) is bounded in $L^\infty(0, T; L^2(\Omega))$. Now, integrating in (A.11) in time and using (A.12) we obtain the following uniform bound for the sequence (∇v_m) :

$$\int_0^T \|\nabla v_m\|_{L^2(\Omega)}^2 dt \leq C \left(\|v_0\|_{L^2(\Omega)}^2 + \|h\|_{L^2(0, T; H^{-1}(\Omega))}^2 \right), \quad (\text{A.13})$$

with $C > 0$ independent of m .

- *Step 3: Bound of the time derivative.* Let us define the operator $\mathcal{A}u := -\operatorname{div}((a + bi)\nabla u)$, which is continuous from $H_0^1(\Omega)$ to $H^{-1}(\Omega)$. Then, from the Galerkin equation (A.9) viewed in $H^{-1}(\Omega)$, we have

$$\|\partial_t v_m\|_{L^2(0, T; H^{-1}(\Omega))} \leq C \left(\|v_m\|_{L^2(0, T; H_0^1(\Omega))} + \|v_m\|_{L^2(0, T; L^2(\Omega))} + \|h\|_{L^2(0, T; H^{-1}(\Omega))} \right). \quad (\text{A.14})$$

This shows that $(\partial_t y_m)$ is a bounded sequence in $L^2(0, T; H^{-1}(\Omega))$ uniformly in m .

- *Step 4: Compactness and passage to the limit.* By the uniform bounds (A.12) (A.13) and (A.14), we deduce that (y_m) is bounded in $L^2(0, T; H_0^1(\Omega)) \cap H^1(0, T; H^{-1}(\Omega))$. Now, by Aubin-Lions lemma implies (after extracting a subsequence, still denoted y_m) that

$$v_m \rightharpoonup v \text{ in } L^2(0, T; H_0^1(\Omega)), \quad v_m \rightarrow v \text{ in } L^2(0, T; L^2(\Omega)), \quad \partial_t v_m \rightharpoonup \partial_t v \text{ in } L^2(0, T; H^{-1}(\Omega)). \quad (\text{A.15})$$

Now, by (A.15) and the assumptions (A.5) and (A.6) on the coefficients α, β, q and passing to the limit in (A.9), we see that v satisfies the variational formulation (A.3) for every $\varphi \in H_0^1(\Omega)$ and almost everywhere on $t \in (0, T)$. The condition (A.4) follows from the fact that $v \in C^0([0, T]; L^2(\Omega))$ (by standard Lions theorems) and the fact that $P_m v_0 \rightarrow v_0$ in $L^2(\Omega)$.

The uniqueness follows from (A.3) and Gronwall's inequality. This completes the proof of Proposition A.2. □

Proposition A.3. *Let $\Omega \subset \mathbb{R}^N$ be a bounded domain with C^2 boundary and let $T > 0$. Assume that the coefficients α and β satisfy*

$$\alpha, \beta \in W^{1, \infty}(\Omega; \mathbb{R}), \quad \alpha(x) \geq \alpha_0 > 0 \text{ almost everywhere in } \Omega. \quad (\text{A.16})$$

Moreover, consider (A.6), $v_0 \in H_0^1(\Omega)$ and $h \in L^2(0, T; L^2(\Omega))$. Then, there exists a strong solution v of (A.1) satisfying

$$v \in H^1(0, T; L^2(\Omega)) \cap C^0([0, T]; H_0^1(\Omega)) \cap L^2(0, T; H^2(\Omega) \cap H_0^1(\Omega)).$$

Moreover, there exists a constant $C > 0$ depending only on α_0 , $\|\alpha\|_{W^{1,\infty}}$, $\|\vec{\sigma}\|_{L^\infty}$, $\|p\|_\infty$, Ω and T such that

$$\begin{aligned} & \|v\|_{L^2(0,T;H^2(\Omega))} + \|v\|_{C^0([0,T];H_0^1(\Omega))} + \|\partial_t v\|_{L^2(0,T;L^2(\Omega))} \\ & \leq C \left(\|h\|_{L^2(0,T;L^2(\Omega))} + \|v_0\|_{H_0^1(\Omega)} \right). \end{aligned}$$

The higher regularity of strong solutions is particularly relevant for numerical analysis. It guarantees that discretizations based on finite differences or finite elements converge to the exact solution, justifying the use of the numerical schemes implemented in Section 4.

Proof. We argue by the Galerkin method.

- *Step 1: Galerkin approximations.* Let $(w_k)_{k \in \mathbb{N}}$ be the Dirichlet Laplacian eigenfunctions. For $m \in \mathbb{N}$, we define the finite-dimensional space $V_m := \text{span}\{w_1, \dots, w_m\}$ and set

$$v_m(t) = \sum_{k=1}^m c_k^{(m)} w_k,$$

which solves the following finite-dimensional system

$$\langle \partial_t v_m, \varphi \rangle_{H^{-1}, H_0^1} + \int_{\Omega} (\alpha + \beta i) \nabla v_m \cdot \nabla \bar{\varphi} \, dx + \int_{\Omega} (\vec{\sigma} \cdot \nabla v_m + p v_m) \bar{\varphi} \, dx = \int_{\Omega} f \bar{\varphi} \, dx, \quad \forall \varphi \in V_m, \quad (\text{A.17})$$

where we know that by Proposition A.2 that for each $m \in \mathbb{N}$,

$$v_m \in L^\infty(0, T; L^2(\Omega)) \cap L^2(0, T; H_0^1(\Omega)). \quad (\text{A.18})$$

- *Step 2: Energy estimates.* Taking $\varphi = \partial_t y_m$ in (A.17) and taking real part, we have

$$\begin{aligned} & \|\partial_t v_m\|_{L^2(\Omega)}^2 + \Re \int_{\Omega} (\alpha + \beta i) \nabla v_m \cdot \nabla \bar{\partial_t v_m} \, dx + \Re \int_{\Omega} (\vec{\sigma} \cdot \nabla v_m + p v_m) \bar{\partial_t v_m} \, dx \\ & = \Re(f, \partial_t v_m). \end{aligned} \quad (\text{A.19})$$

Now, integrating by parts in time, using the fact that α is time-independent and by Young's inequality, we have for a.e. $t \in (0, T)$:

$$\begin{aligned} & \|\partial_t v_m(t)\|_{L^2}^2 + \frac{1}{2} \|\sqrt{\alpha} |\nabla v_m(t)|\|_{L^2}^2 \\ & \leq \|\vec{\sigma}\|_{L^\infty} \|\nabla v_m(t)\|_{L^2} \|\partial_t v_m(t)\|_{L^2} \|\partial_t v_m(t)\|_{L^2} + \|p\|_{L^\infty} \|v_m(t)\|_{L^2} \|\partial_t v_m(t)\|_{L^2} \\ & \quad + \|h(t)\|_{L^2} \|\partial_t v_m(t)\|_{L^2} \\ & \leq \frac{1}{2} \|\partial_t v_m(t)\|_{L^2}^2 + \left(\frac{3}{2\alpha_0} \|\vec{\sigma}\|_{L^\infty}^2 + \frac{3}{2\alpha_0 C_p} \|p\|_{L^\infty}^2 \right) \|\sqrt{\alpha} |\nabla v_m(t)|\|_{L^2}^2 + \frac{3}{2} \|h(t)\|_{L^2}^2, \end{aligned}$$

where $C_p > 0$ is the constant appeared in the Poincaré's inequality. This means that for a.e. $t \in (0, T)$ we have

$$\|\partial_t v_m(t)\|_{L^2}^2 + \frac{d}{dt} \|\sqrt{\alpha} |\nabla v_m(t)|\|_{L^2}^2 \leq \gamma_2 \|\sqrt{\alpha} |\nabla v_m(t)|\|_{L^2}^2 + 3\|h(t)\|_{L^2}^2, \quad (\text{A.20})$$

where $\gamma_2 := \frac{3}{\alpha_0} (\|\sigma\|_{L^\infty}^2 + C_p^{-1} \|q\|_{L^\infty}^2)$. By Gronwall's inequality, we have

$$\|\sqrt{\alpha} |\nabla v_m(t)|\|_{L^2}^2 \leq e^{\gamma_2 t} \left(\|\alpha\|_{L^\infty} \|\nabla v_m(0)\|_{L^2}^2 + 3 \int_0^t e^{-\gamma_2 s} \|h(s)\|_{L^2}^2 ds \right), \quad \text{a.e. } t \in [0, T]. \quad (\text{A.21})$$

Moreover, integrating in time in (A.20) and using the estimate (A.21), we deduce that

$$\|\partial_t v_m\|_{L^2(0,T;L^2(\Omega))} \leq C \left(\|v_0\|_{H_0^1(\Omega)} + \|f\|_{L^2(0,T;L^2(\Omega))} \right). \quad (\text{A.22})$$

- *Step 3: Estimates on H^2 .* Let us consider the operator $A : H^2(\Omega) \cap H_0^1(\Omega) \rightarrow L^2(\Omega)$ defined by

$$Au := -\operatorname{div}((\alpha + \beta i) \nabla u) + \vec{\sigma} \cdot \nabla u + pu.$$

Under the assumptions on α , β , $\vec{\sigma}$ and q , A enjoys H^2 -elliptic regularity, i.e., if $g \in L^2(\Omega)$ and $w \in H_0^1(\Omega)$ solves $Aw = g$ in Ω , then $w \in H^2(\Omega) \cap H_0^1(\Omega)$ and we have the following estimate:

$$\|w\|_{H^2(\Omega)} \leq C (\|g\|_{L^2(\Omega)} + \|w\|_{L^2(\Omega)}),$$

where C depends on α_0 , $\|a\|_{W^{1,\infty}}$, $\|b\|_{W^{1,\infty}}$ and Ω . Now, for a.e. $t \in (0, T)$, the Galerkin function $v_m(t) \in V_m$ satisfies, in the strong sense

$$Av_m(t) = g_m(t) := h(t) - \partial_t v_m(t) - \vec{\sigma} \cdot \nabla v_m(t) - p v_m(t).$$

It is clear that $g_m(t) \in L^2(\Omega)$ for a.e. $t \in (0, T)$ and the map $t \mapsto \|g_m(t)\|_{L^2(\Omega)}$ belongs to $L^2(0, T)$ uniformly in m . Now, by elliptic regularity of A , we obtain

$$\|v_m(t)\|_{H^2(\Omega)} \leq C (\|g_m(t)\|_{L^2(\Omega)} + \|v_m\|_{L^2(\Omega)}) \quad \text{a.e. in } (0, T). \quad (\text{A.23})$$

Now, from (A.23), we use the estimates (A.8) and (A.22) to get

$$\|v_m\|_{L^2(0,T;H^2(\Omega))} \leq C \left(\|v_0\|_{H_0^1(\Omega)}^2 + \|h\|_{L^2(0,T;L^2(\Omega))} \right). \quad (\text{A.24})$$

- *Step 4: Last arrangements.* Now, we will analyze the pass to the limit on m . From (A.18), (A.21) and (A.24), we know that

$$(y_m) \text{ is bounded in } L^2(0, T; H^2(\Omega) \cap H_0^1(\Omega)) \cap H^1(0, T; L^2(\Omega)).$$

By Aubin-Lions Lemma (extracting subsequence if necessary) we obtain a limit v with the following properties:

$$v_m \rightharpoonup v \text{ in } L^2(0, T; H^2(\Omega)), \quad v_m \rightarrow v \text{ in } L^2(0, T; H_0^1(\Omega)), \text{ and } \partial_t v_m \rightharpoonup \partial_t v \text{ in } L^2(0, T; L^2(\Omega)).$$

Passing to the limit in (A.17) gives that v is the weak solution and satisfies

$$v \in L^2(0, T; H^2(\Omega) \cap H_0^1(\Omega)), \quad \partial_t v \in L^2(0, T; L^2(\Omega)).$$

In fact, this proves that v is a strong solution of (A.1). Finally, thanks to the above estimates, we conclude that

$$\|v\|_{L^2(0, T; H^2(\Omega) \cap H_0^1(\Omega))} + \|\partial_t v\|_{L^2(0, T; L^2(\Omega))} \leq C \left(\|v_0\|_{H_0^1(\Omega)} + \|h\|_{L^2(0, T; L^2(\Omega))} \right).$$

This ends the proof of Proposition A.3.

□